Applied Physics A (2019) 125:544
https://doi.org/10.1007/s00339-019-2826-z

Applied Physics A
Materials Science & Processing

S.I.: NEW FRONTIERS IN LASER INTERACTION

Femtosecond laser-assisted synthesis of Ni/Au BONs in various alcoholic solvents

Niusha Lasemi[1] · Christian Rentenberger[2] · Robert Pospichal[3] · Alexey S. Cherevan[1] · Martin Pfaffeneder-Kmen[4] · Gerhard Liedl[3] · Dominik Eder[1]

Received: 19 May 2019 / Accepted: 14 July 2019 / Published online: 23 July 2019

Abstract

Crystalline Ni/Au bimetallic oxide nanoparticles with various forms of crystallographic systems and defects were generated by femtosecond laser ablation of nickel–gold target in alcoholic solvents. The nature of the liquid can influence the chemical composition, stability, and size distribution of laser-synthesized nanoparticles. In ethanol, bimodal crystalline bimetallic Ni/Au oxide nanoparticles with median size of 15 nm were synthesized. The laser ablation of Ni/Au target in isopropanol and butanol led to nearly monomodal size distribution with median size of 10 and 13 nm, respectively. High-resolution transmission electron microscopy of Ni/Au oxide nanoparticles in butanol, revealed a graphitic shell of a few atomic layers. In this context, two suggested mechanisms were considered. First of all, the high photon intensity of femtosecond laser pulses can induce direct photolysis of liquid media. Secondly, the formation of supercritical temperature solvent due to the interaction of solvent with molten metal layer at liquid–metal interface can trigger pyrolysis of solvent. These mechanisms can contribute to butanol decomposition and encapsulation of Ni/Au oxide bimetallic nanoparticles with graphite shell. Graphite shell can create a better colloidal stability by preventing nanoparticles from further growth and agglomeration.

1 Introduction

Pulsed laser ablation in liquids is an auspicious green technology to synthesize highly pure nanomaterials for various applications (i.e., biomedicine, energy conversion, catalysis) [1–3]. The laser-assisted assembly of colloidal nanomaterials in liquids involves numerous procedures taking place in the bulk, interfacial region and in the molten layer of material during an extended time period from femtoseconds up to milliseconds [4–15]. Furthermore, physicochemical processes take place in timescales similar to the natural oscillation times of atoms and molecules from femtosecond (10^{-15} s) to picosecond regime (10^{-12} s) [16]. Ultrafast laser systems with their unique characteristics such as short pulse durations and high peak intensities have attracted more attention for both fundamental and practical research and applications [17–19].

Ultrashort pulse laser materials processing led to a thermal non-equilibrium condition between electrons and lattice that was previously described by two-temperature model (TTM) [20, 21]. Additionally, high-intensity ultrashort laser ablation in liquids presented a localized synthesis technique that may lead to higher ablation efficiency [22], as the whole laser energy contributed to photon–electron interactions due to insignificant lattice motion and heat diffusion [23].

Furthermore, as pulse duration is much shorter than the electron-lattice relaxation time (10^{-10} to 10^{-12} s) [16, 24], the heat affected zone (HAZ) can proficiently be suppressed [15, 25]. In fact, the heat accumulation matter is insignificant for laser frequency repetition rates $f_{\text{rep}} \leq 200$ kHz [26].

Femtosecond laser ablation of Au target in deionized water revealed two suggested mechanisms; cold ablation at relatively low laser fluences which led to monodispersed colloidal solutions and plasma-induced heating of the target that triggered the formation of larger particles

✉ Niusha Lasemi
niusha.lasemi@tuwien.ac.at

[1] Institute of Materials Chemistry, Vienna University of Technology, Getreidemarkt 9, 1060 Vienna, Austria

[2] Center for Nanostructure Research, Faculty of Physics, University of Vienna, Boltzmanngasse 5, 1090 Vienna, Austria

[3] Institute for Production Engineering and Laser Technology, Vienna University of Technology, Getreidemarkt 9, 1060 Vienna, Austria

[4] Department of Physical Chemistry, University of Vienna, Wahringer 42, 1090 Vienna, Austria

and polydispersities at higher fluences [6]. The elemental analysis of laser-synthesized core–shell Fe/Au nanoparticles in liquids disclosed the chemical interactions of the particle surface with liquid media [27]. In fact, the nonlinear energy absorption may initiate the photoionization of solvent due to the interaction of ultrashort laser pulses with liquid media [28]. Laser-induced photoionization processes can be responsible for laser energy losses due to the interaction of laser light with liquid media particularly for laser pulses ≤ 150 fs [29]. Laser-induced optical breakdown can occur in a transparent dielectric environment when the number of free electron density goes beyond its critical value of 10^{18}–10^{20} cm^{-3} [30, 31]. The time-of-flight mass spectroscopy confirmed the direct photolysis of acetone molecules by femtosecond laser pulses (@800, 90 fs, 1 kHz) and the formation of a mixture of polyynes with variable chain lengths and graphitic species [32]. In this regard, the non-equilibrium nature of femtosecond laser pulses, nonlinear processes, local thermalization, and the type of liquid media surrounding the target are significant factors to manipulate the shape, size distribution, and internal phase composition of nanoparticles [27, 32, 33].

Designing nanomaterials with enhanced physicochemical properties is of importance. Bimetallic nanomaterials can reveal interesting properties in contrast to single metallic nanoparticles [34]. Bimetallic alloy nanomaterials have shown precious properties in a variety of applications, Ag/Cu nano alloys were employed as highly active catalysts [35]; Au/Fe [34] and Ag/Au [36] due to the enhancement of optical and magnetic behaviors have shown a potential for medical applications. Pt/Au nano alloys were used to produce fuel cell electro-catalysts [37]. A wide variety of Ni-based alloys were used in medical sciences, especially in dentistry and implantology due to their biocompatibility, good mechanical properties, and chemical resistivity [38]. Moreover, Ni/Au alloys have shown high potential in catalysis; increasing O_2 reactivity [39], and hydrogenation of aromatic nitro compounds [40, 41]. The mechanism of femtosecond laser generation of nanomaterials in liquid was explained by atomistic modeling of laser ablation of Ag film in water [42]. The rapid cooling and condensation of primary nanoparticles initiated the formation of primary particles with the average size of 10 nm. Secondary nanoparticles around 50 nm were formed due to the destruction of superheated molten metal layer at plume–liquid interface [42]. In this work, the single step eco-friendly synthesis of Ni/Au bimetallic oxide nanoparticles (BONs) by femtosecond laser ablation in various alcoholic solvents is presented. Furthermore, the effect of solvent nature on the chemical composition, crystallinity, and size distribution of Ni/Au BONs is explained.

2 Experimental

Target materials; nickel (50 × 50 × 0.5 mm) with purity of ≥ 99.5% and gold wire (purity ≥ 99.95%) for physical vapour deposition (PVD) were provided from Alfa Aesar Company. Solvents were ethanol, butanol, and isopropanol (Sigma-Aldrich; p.a.). These platelets were cleaned by ultra-sonication in ethanol. Au was coated on Ni target via PVD [43]. The thickness of Au on Ni was measured by the time-of-flight secondary ion mass spectrometry IONTOF (ToF-SIMS^5). The estimated thickness of gold is about 50 nm. Target was positioned at the bottom of the glass cell with the height of 15 mm. An optical window for the horizontal access of laser beam was placed (Fig. 1).

Horizontal beam delivery was preferred to decrease the optical fluctuations due to vapor bubble formation.

Nanoparticle production was carried out using a femtosecond titanium–sapphire (Ti:sapphire) laser setup with various sections including oscillator, pulse stretcher, amplifier, and pulse compressor. A commercial femtosecond laser system was employed as the seeding laser system, emitting at the wavelength of 800 nm (SPECTRA-PHYSICS®, ≤ 400 mW, pulse duration 10 fs, repetition rate of 75 MHz and beam diameter ca. 6 mm). So-called chirped pulse amplification (CPA) [44] was applied before transferring seed laser pulses to the Pockels cell. CPA technique includes the temporal stretching of ultra-short pulses with a large spectral bandwidth provided by an oscillator. Therefore, the intensity of pulse is considerably decreased to avoid nonlinear optical effects which cause damage to optical components, amplifier and distortion of temporal and spatial pulse profile [45]. Laser pulses from oscillator entering stretching part after passing through the Faraday isolator (FI) to prevent back-reflections from amplifier to oscillator and changing horizontally polarized beam to vertically polarized one. The specific number of beam reflections were operated between two pairs of third-order dispersion pre-compensating mirrors (TOD-1/2 and TOD-3/4). Subsequently, laser beam went through a main pulse stretcher (PS1), reflected by an adaptive secondary mirror (ASM) and guided into the amplifying part. Amplified laser pulses with pulse duration of 30 fs and repetition rate of 1 kHz were generated. Pulse duration was measured by autocorrelation technique [46]. Three iris diaphragms (A1–A3) were used to make a beam path toward prism compressor. Powermeter (OPHIR Photonics) was positioned after diaphragm A3. Maximum output power for system was ≤ 1 W. Focus position in various liquid media was experimentally evaluated by microscopically measuring ablated area on a silicon target (ImageJ software) as a function of the distance of focusing parabolic mirror (focal length

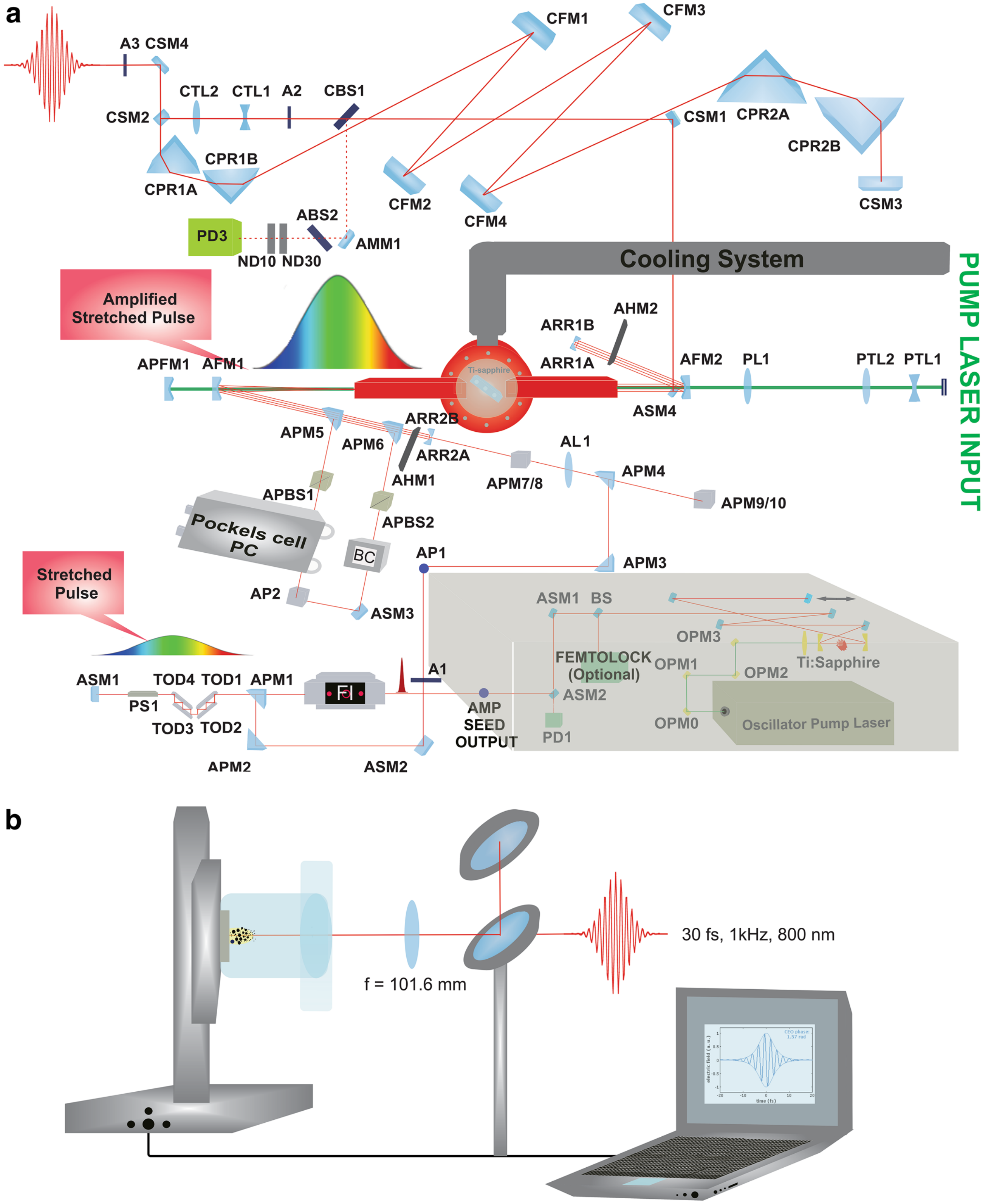

Fig. 1 **a** The schematic of femtosecond Ti:sapphire laser; seed laser (10 fs, 75 MHz, 800 nm, 400 mW) and amplifying system (30 fs, 800 nm, 1 kHz, 800 mW) pumping with Nd:YAG laser and **b** nanoparticle synthesis setup; the system connected to the motorized *XYZ*-scanning stage controlled via CNC program

Table 1 Final pulse duration after passing through liquids

Solvents	Δt_{out}/fs
Ethanol	65
Isopropanol	94
Butanol	117

101.6 mm). The Gaussian beam radius of 87 mm was evaluated. The squared diameter of damaged zone (D^2) evaluated by optical microscopy is correlated to Gaussian beam radius (w_0), pulse energy, (E) and threshold pulse energy (E_{th}) [47]. Laser beam is supposed to have a Gaussian beam distribution:

$$D^2 = 2w_0^2 \ln\left(\frac{E}{E_{\mathrm{th}}}\right). \tag{1}$$

Pulse energy E and peak fluence F are related by:

$$F = \frac{2E}{\pi w_0^2}. \tag{2}$$

Equation (3) was employed to calculate final pulse duration after passing through liquids [48]:

$$\Delta t_{\mathrm{out}} = \sqrt{\Delta t^2 + \left[4 \ln 2 \frac{(\mathrm{GDD})}{\Delta t}\right]^2}, \tag{3}$$

where Δt_{out} is final pulse duration and GDD is group delay dispersion. The final pulse duration in various solvents are shown in Table 1.

Ni/Au BONs were analysed using various transmission electron microscopy (TEM) methods. Selected area electron diffraction pattern (SAED), bright and tilted dark-field images of laser-synthesized nanoparticles were obtained by a Philips CM200 TEM (LaB6 cathode, acceleration voltage of 200 kV) equipped with a Gatan Orius CCD camera. The phase identification and crystallographic data analysis of Ni/Au BONs were done by AtomWork database [49]. Number-weighted size distributions were evaluated from at least seven TEM frames (700 × 700 nm) using microscopy software (Gatan, Inc.). Energy-dispersive X-ray spectroscopy (EDX) in connection with TEM was used for chemical composition studies. TEM samples were prepared by placing several droplets of colloidal dispersion (after 5 min ultrasonic irradiation) on a carbon-film-coated cop-per grid followed by solvent evaporation in air at room temperature. High-resolution transmission electron microscopy (HRTEM) was performed with the FEI Titan 80-300 equipped with an imaging Cs-corrector.

3 Results and discussion

Laser fluence F was chosen around 1 J cm^{-2} to decrease energy losses during the synthesis. Laser-induced persistent bubble formation due to the evaporation of solvent [50, 51] can scatter and shield laser energy and subsequently lower productivity. The nonlinear effect; so-called filamentation of ultrashort pulsed laser beam in fluids at higher fluences can also participate in energy losses [52]. Additionally, to have a better productivity, the number of pulses $N = 1000$ was applied. TEM bright-field image of Ni/Au BONs in ethanol with respective EDX analyses is presented in Fig. 2. The EDX study of the sample showed mainly nickel, oxygen and very low concentration of Au. The EDX spectrum of area (a) marked in the bright-field image is related to the supporting matrix which is dominated by the siloxane glue contaminations (Si and O, Fig. 2a).

The high Cu signal is a consequence of stray electrons hitting the Cu support grid. The EDX spectrum of Fig. 2b represents the signal of the imaged sample area containing nanoparticles.

The number-weighted size distribution study of femtosecond laser-generated Ni/Au BONs in ethanol and respective evaluated results are shown in Fig. 3 and Table 2. Bimodal size distribution was observed. The highest frequency of particles presented a median diameter around 15 nm and minor mode could be distinguished in the tail at larger sizes.

Due to the positively skewed lognormal size distribution, median size with interquartile range (IQR) is presented.

Essentially, Q_1 (quartile 1) and Q_3 (quartile 3) are correlated to 25% and 75% of the lognormal size distribution graph, respectively; hence, IQR can be measured by substracting Q_1 from Q_3 value [53].

IQR for lognormal fit function and standard deviation for Gaussian fit function can correlate to the level of polydispersity of colloidal nanoparticles.

The multimodality of laser-synthesized nanoparticles may be related to the cavitation bubble dynamic, growth and collapse. In fact, the primary particles of 8–10 nm came from the expulsion of vaporized atoms during bubble growth as they dispersed inside and outside of cavitation bubble due to the permeability of liquid–bubble interface [54, 55]. Moreover, the agglomeration of primary nanoparticles during bubble collapse may trigger the formation of secondary nanoparticles around 30–60 nm [54–56]. Not only the agglomeration but also the rupture of superheated molten metal layer under supercritical liquid may play a role in the formation of secondary nanoparticles [42]. For structural analysis; SAED pattern and dark-field images (a–e) were taken (cf. Fig. 4). The resulting crystallographic data of Ni/Au BONs in ethanol are shown in Table 3. Crystallographic data are obtained by calculating

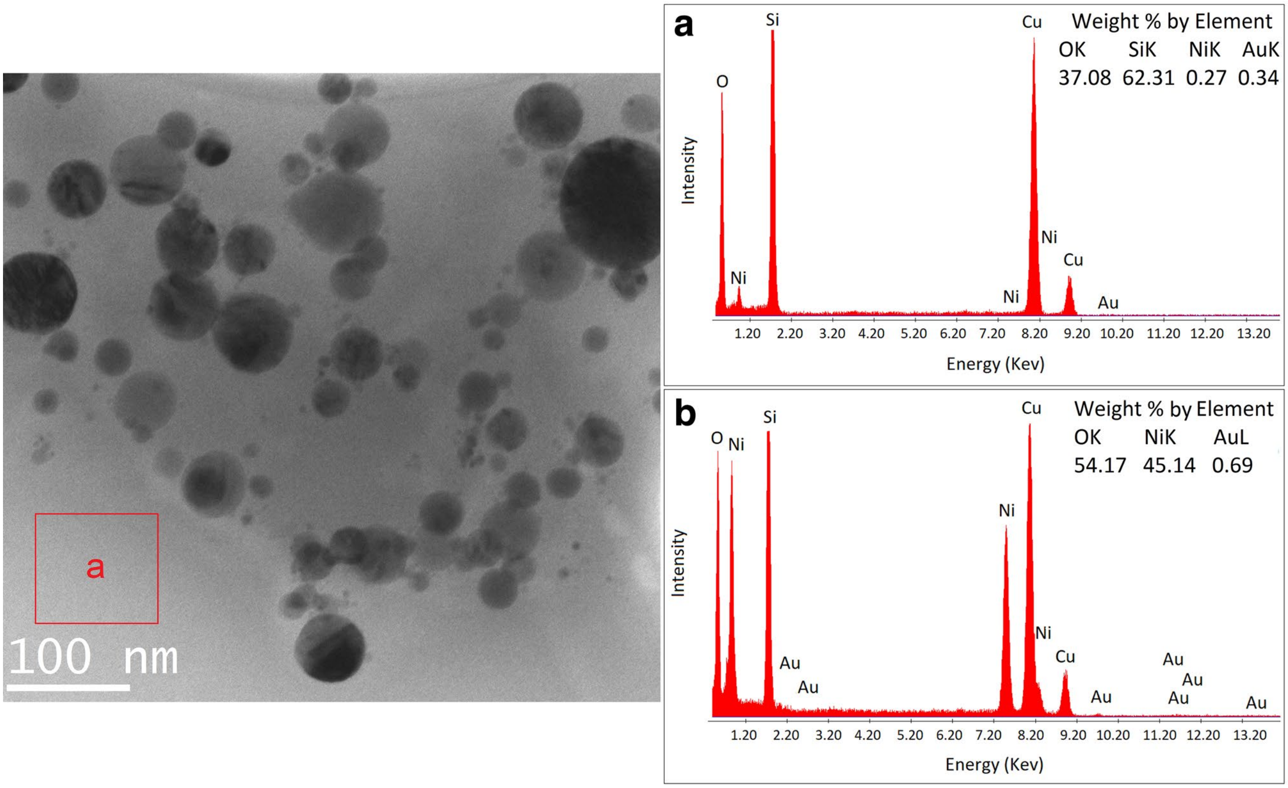

Fig. 2 TEM bright-field image and the EDX results of femtosecond laser-synthesized (1 kHz, 800 nm) Ni/Au BONs; **a** matrix area and **b** the whole area containing nanoparticles (ethanol, $N = 1000$ and $F = 1$ J cm^{-2})

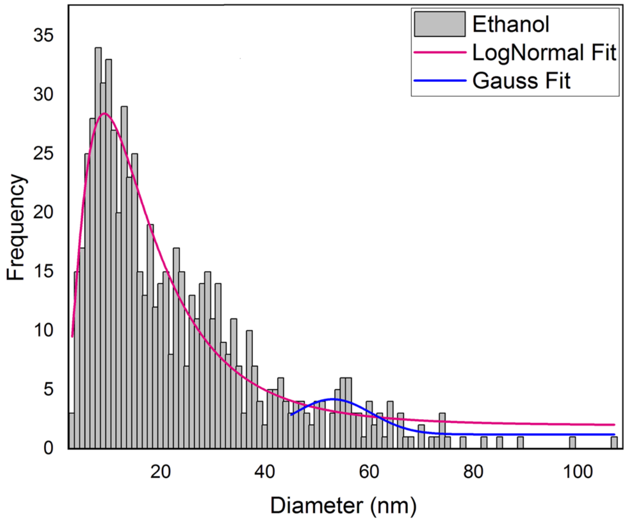

Fig. 3 The number-weighted particle size distribution of Ni/Au BONs in ethanol ($N = 1000$ and $F = 1$ J cm^{-2})

Table 2 The fitting results of number-weighted size distribution (Ni/Au BONs in ethanol, $N = 1000$ and $F = 1$ J cm^{-2})

1st fit	Median, nm	IQR
Lognormal	15	3.35
2nd fit	Mean, nm	Standard deviation
Gauss	53	7.38

reciprocal lattice distances using PASAD-tools [57] and comparing measured lattice distances with a database [49]. To be precise, all crystal system possibilities related to the calculated lattice distances are given. Dark-field images are obtained using a contrast aperture in the diffraction plane at different positions along the first and second rings (e.g., position A).

The presented dark-field images (Fig. 4a–e) correspond to the first and second rings that are related to hexagonal Ni and monoclinic NiO_2 with lattice distances of 0.216 and 0.197 nm, respectively (Table 3). In fact, due to the close distance of the first and second rings, the intensity contributions from different structures cannot be avoided.

The observed contrast originates from various atomic orientations of nanoparticles and crystalline defects (i.e., stacking fault SF) common for cubic and hexagonal systems. One can assume, the laser fluence of 1 J cm^{-2} is adequately high to make longer melting periods and slower resolidification processes. This can trigger the evolution of crystalline structures [15, 58]. Additionally, Ni/Au binary phase diagram showed an immiscible

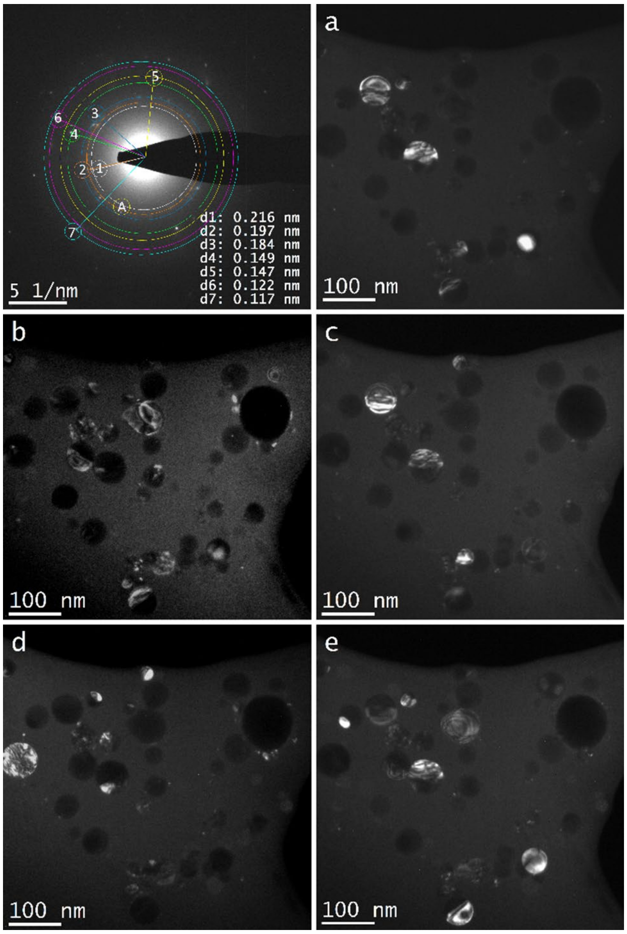

Fig. 4 The laser-synthesized Ni/Au BONs in ethanol. ($N = 1000$, $F = 1$ J cm^{-2}). SAED pattern (upper left) and the dark-field images of the same area using different diffracted electron beams along the 1st and 2nd rings (**a**–**e**)

region at temperatures below 500 K [59]. As temperature of plasma plume where nucleation starts for femtosecond pulses are typically between 5000 and 7000 K even at lower energy fluences [10, 60], phase segregation and core–shell formation of Ni/Au were impossible whereas plasma environment was suitable for nanocomposite formations.

The TEM bright-field image of Ni/Au BONs in isopropanol and the corresponding EDX spectrum are presented in Fig. 5. The EDX study of nanoparticles showed mainly nickel, gold and oxygen.

The number-weighted size distribution study of Ni/Au BONs in isopropanol demonstrated the decreasing of IQR, median diameter and subsequently polydispersity compared to ethanol solvent (Fig. 6, Table 4).

While there was not a clear graphite shell around laser-synthesized nanoparticles in isopropanol, one could suggest that the steric stabilization of colloidal Ni/Au BONs came from the existence of amorphous carbonaceous networks [61] due to the laser-induced photolysis and pyrolysis of isopropanol solvent.

A bright-field image, the corresponding diffraction pattern and dark-field images of the same area are shown in Fig. 7. Crystallographic data obtained from the analyses of diffraction pattern are listed in Table 5.

In analogy to ethanol, crystalline Ni/Au metallic and oxide nanoparticles of various phases are identified (Table 5). Dark-field images (cf. Fig. 7a–d) were taken using various tilting angles of the electron beam and selecting the intensity along the first and second rings (e.g., position A in the diffraction pattern). Due to the closely spaced rings these images display particles that can be assigned to the hexagonal Ni and monoclinic NiO_2 structure with lattice distances of 0.216 nm and 0.197 nm, respectively. In addition, the contrast demonstrates that most of the particles show linear features related to planar defects.

In Fig. 8, TEM bright-field image of Ni/Au BONs in butanol and the corresponding EDX spectrum are shown. The EDX study reveals that the nanoparticles contain mainly nickel and low concentrations of gold and oxygen. The oxidation of nanoparticles is decreased in contrast to ethanol medium and in analogy to isopropanol.

Table 3 The laser-synthesized Ni/Au BONs in ethanol, selected area diffraction pattern results, corresponding crystallographic data and phase identifiers. ($N = 1000$, $F = 1$ J cm^{-2})

Material	Crystal system	Lattice distance, nm	Miller indices	Pearson symbol	Space group	Space group number
Ni	Hexagonal	0.216	[002]	hP2	$P6_3/mmc$	194
NiO_2	Monoclinic	0.197	[200]	mS6	P-3m1	12
Au_2O_3	Orthorhombic	0.184	[022]	oF40	Fdd2	43
Au_2O_3	Orthorhombic	0.149	[551], [371]	oF40	Fdd2	43
NiO	Cubic	0.147	[220]	cF8	Fm-3m	225
NiO	Monoclinic	0.147	[111]	mS4	C2/m	12
NiO	Hexagonal	0.147	[110], [104]	hR6	R-3m	166
Au	Cubic	0.122	[311]	cF4	Fm-3m	225
Ni	Hexagonal	0.122	[103]	hP2	$P6_3/mmc$	194
Au	Cubic	0.117	[222]	cF4	Fm-3m	225

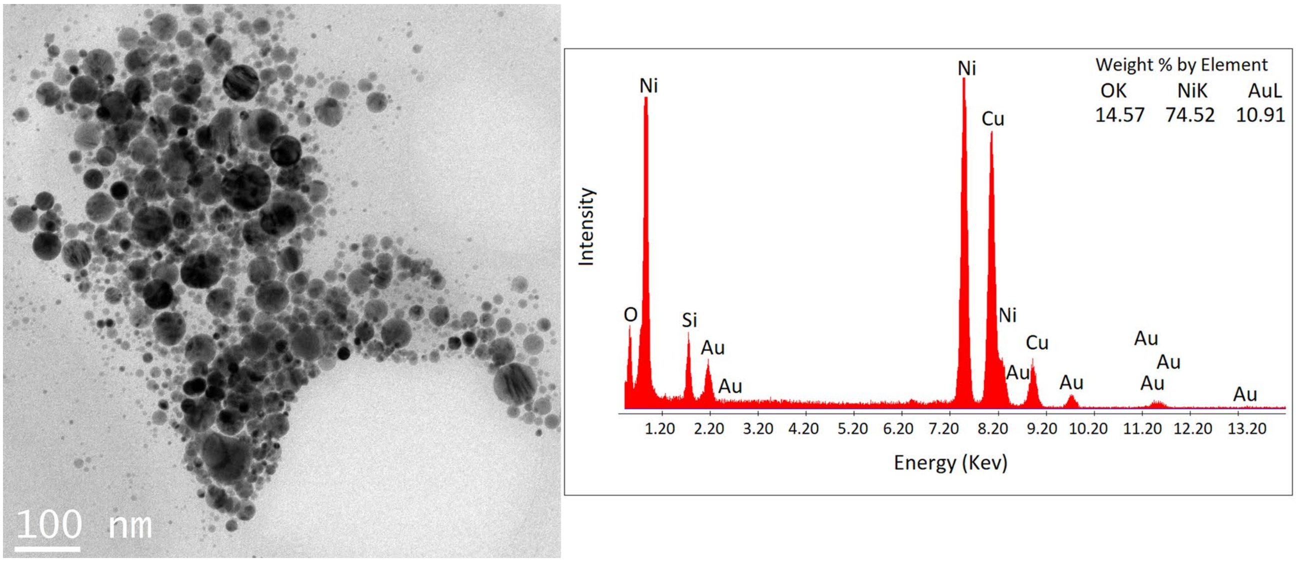

Fig. 5 TEM bright-field image and the EDX results of femtosecond laser-synthesized (1 kHz, 800 nm) of Ni/Au BONs (isopropanol, $N = 1000$ and $F = 1$ J cm^{-2})

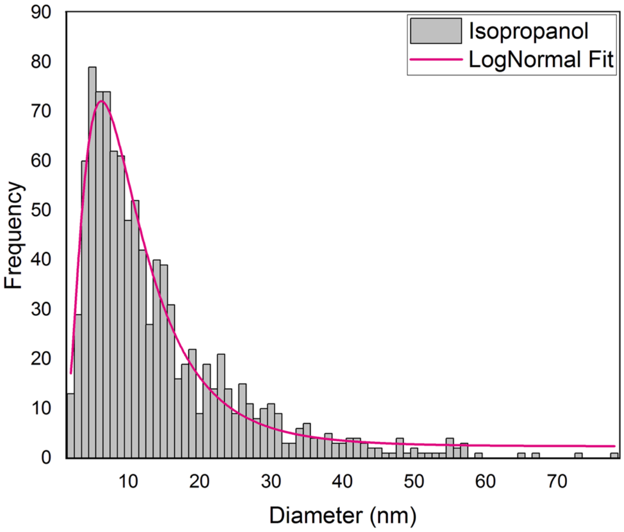

Fig. 6 The number-weighted particle size distribution of Ni/Au BONs in isopropanol ($N = 1000$ and $F = 1$ J cm^{-2})

Table 4 The fitting results of number-weighted size distribution (Ni/Au BONs in isopropanol, $N = 1000$ and $F = 1$ J cm^{-2})

Curve fitting	Median, nm	IQR
Lognormal	10	1.12

Number-weighted size distribution calculated from the bright-field images of Ni/Au BONs in butanol showed smaller median size and lower IQR in contrast to ethanol medium and similar to isopropanol (Fig. 9, Table 6).

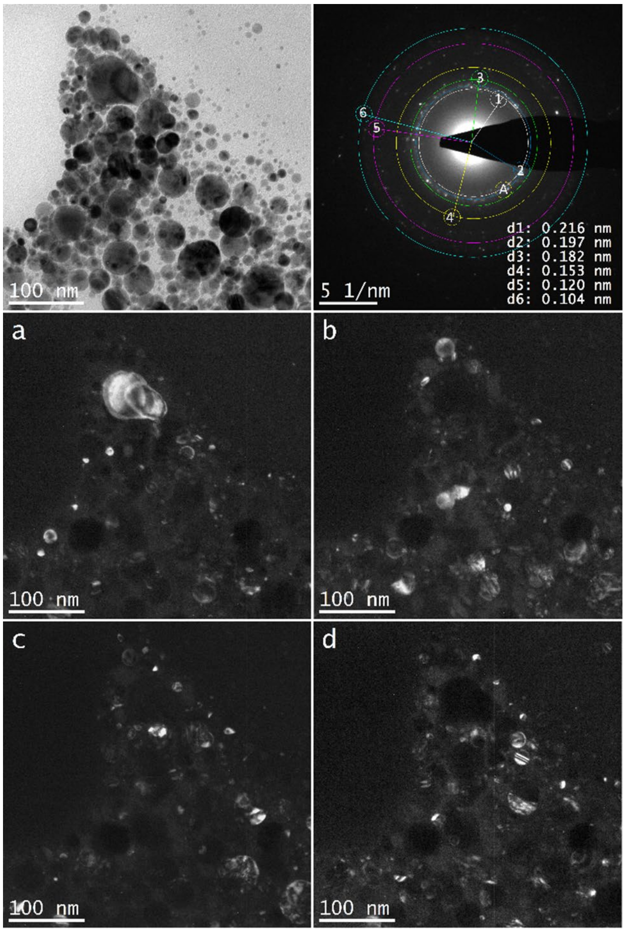

Fig. 7 The laser-synthesized Ni/Au BONs in isopropanol ($N = 1000$, $F = 1$ J cm^{-2}). Bright-field image (upper left), SAED (upper right) and dark-field images at various tilting angles of the electron beam along the 1st and 2nd rings (**a**–**d**)

Table 5 The laser-synthesized Ni/Au BONs in isopropanol, selected area diffraction pattern results, corresponding crystallographic data and phase identifiers ($N = 1000$, $F = 1\ \mathrm{J\ cm^{-2}}$)

Material	Crystal system	Lattice distance, nm	Miller indices	Pearson symbol	Space group	Space group number
Ni	Hexagonal	0.216	[002]	hP2	$P6_3/mmc$	194
NiO_2	Monoclinic	0.197	[200]	mS6	P-3m1	12
Au_2O_3	Orthorhombic	0.182	[351], [511]	Fdd2	oF40	43
Au_2O_3	Orthorhombic	0.153	[640], [280]	Fdd2	oF40	43
NiO	Monoclinic	0.120	[220], [002]	mS4	C2/m	12
NiO	Hexagonal	0.120	[202], [006]	hR6	R-3m	166
Ni	Hexagonal	0.120	[024]	hR6	R-3m	166
Ni	Cubic	0.104	[222]	cF4	Fm-3m	225

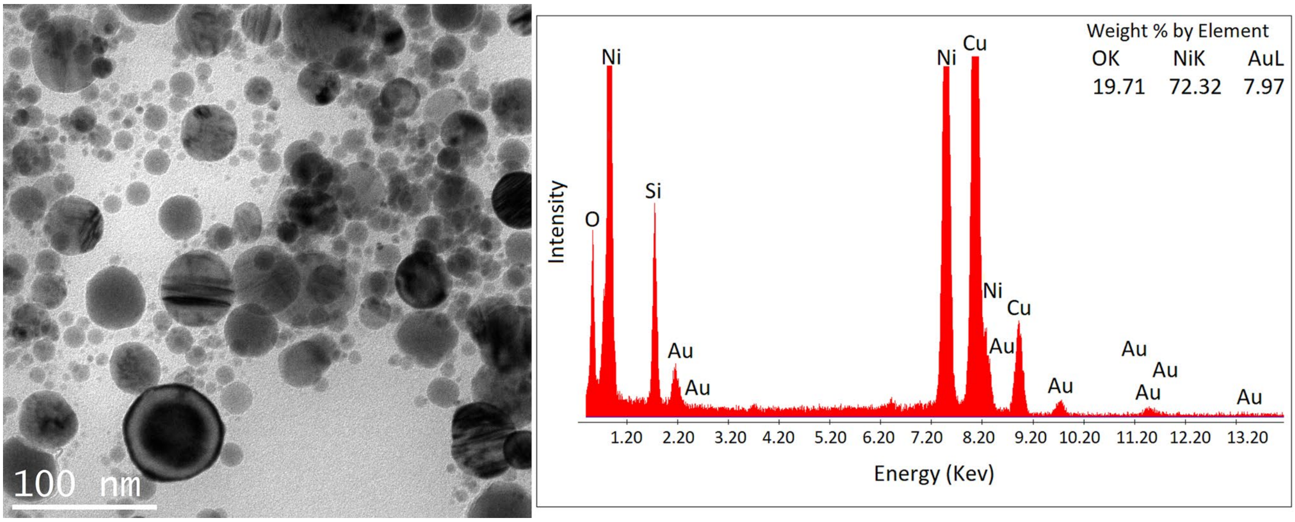

Fig. 8 TEM bright-field image and the EDX results of femtosecond laser-synthesized (1 kHz, 800 nm) of Ni/Au BONs (butanol, $N = 1000$ and $F = 1\ \mathrm{J\ cm^{-2}}$)

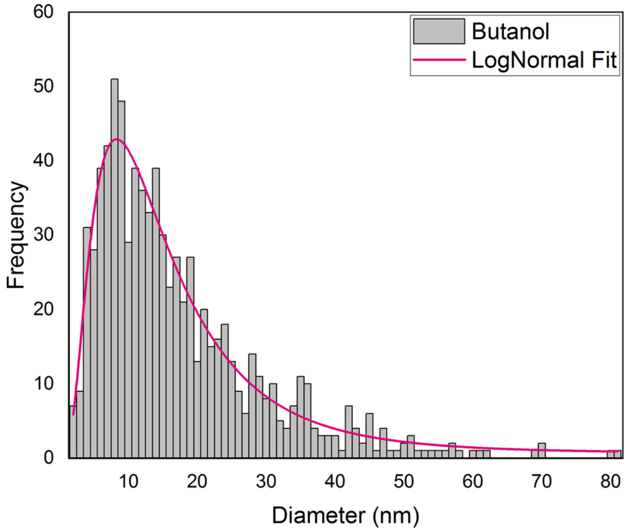

Fig. 9 The number-weighted particle size distribution of Ni/Au BONs in butanol ($N = 1000$ and $F = 1\ \mathrm{J\ cm^{-2}}$)

Table 6 Fitting results of number weighted size distribution (Ni/Au BONs in butanol, $N = 1000$ and $F = 1\ \mathrm{J\ cm^{-2}}$)

Curve fitting	Median, nm	IQR
Lognormal	13	2.33

A SAED pattern and dark-field images acquired using intensities along the first and second rings are displayed in Fig. 10. The measured reciprocal lattice distances and respective dark-field images (Fig. 10a–e) of the Ni/Au BONs synthesized in butanol revealed the existence of crystalline Ni/Au metallic and oxide nanoparticles of different phases containing various crystallographic defects (Table 7). The presented dark-field images are related to lattice distances of 0.216 and 0.203 nm that can be correlated to cubic Au and hexagonal Ni, respectively (cf. Table 7).

High-resolution electron microscopy of laser-synthesized Ni/Au BONs in butanol as shown in Fig. 11 discloses that

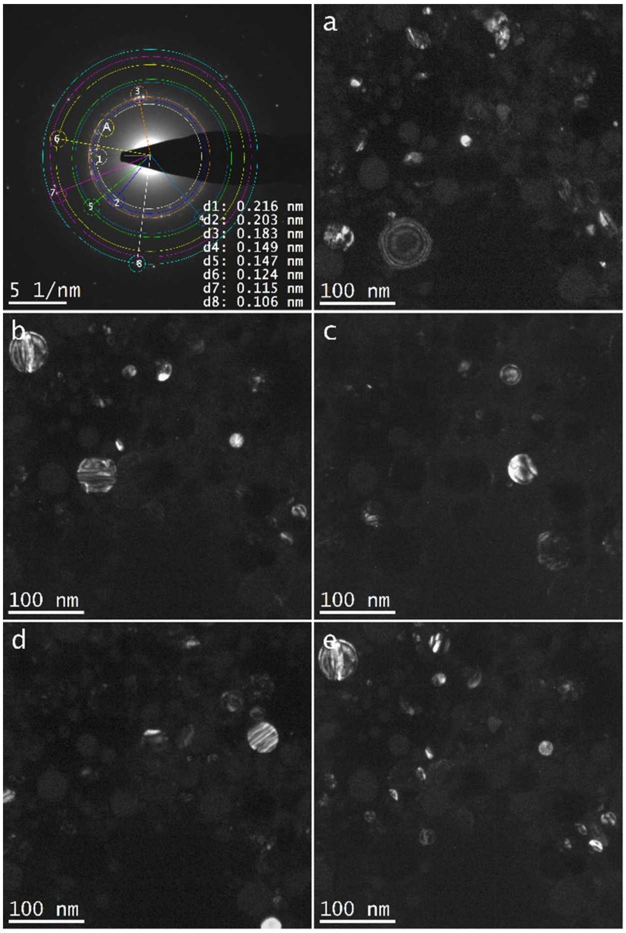

Fig. 10 The laser-synthesized Ni/Au BONs in butanol. ($N = 1000$, $F = 1$ J cm^{-2}). SAED (upper right) and respective dark-field images at various tilting angles of the electron beam along the 1st and 2nd rings (**a**–**e**)

core–shell structures are present. The observed fringes with the lattice distance of 0.334 nm can be correlated to crystalline graphite with a few atomic layer of thickness. In addition, atomically resolved images of the core confirm the presence of particles with hexagonal crystal structure.

The plasma plume generated in tens of femtoseconds of the laser pulse [62]. In fact, plasma environment can initiate nanomaterial manipulation, as the high-intensity laser beam at the focused laser spot on the target at the solid–liquid interface can generate a high concentration of reactive species [30, 63, 64]. Additionally, highly intense femtosecond laser pulse interaction with solvents can induce photolysis [30, 32]. The photoionization of butanol solvent can generate carbonaceous products, these carbonaceous species may deposit on primary nanoparticles that were produced at the beginning of the bubble evolution and create core–shell structures. Typically the interaction of laser beam with solvent molecules with higher carbon contents, such as butanol, acetone, *n*-hexane and toluene, results in the graphitization of synthesized nanoparticles [32, 61, 65–68].

Furthermore, the interaction of hot metallic surface with liquid media may play a role in pyrolysis of solvent molecules [12] as liquid can reach its supercritical temperature due to the contact with molten metal layer [42]. Moreover, nickel is a proficient catalyst for carbonization [69]. Laser interaction with nickel target in butanol solvent showed an increase in the incubation behavior of nickel target due to the thermal decomposition of solvent molecules, deposition of carbonaceous species on ablated craters, and increased absorptivity [12, 70]. The general thermal decomposition of *n*-butanol follows the equation (4) [12, 71]:

$$C_4H_{10}O \rightarrow CO + 2CH_4 + H_2 + C \tag{4}$$

The smaller median diameter of Ni/Au BONs in isopropanol and butanol in contrast to ethanol medium indicates the existence of graphite shell. This can bring more colloidal stability and may prevent nanoparticles from further growth, coalescence and Ostwald ripening processes [61, 72].

4 Conclusions

Femtosecond laser ablation of Ni/Au target in various alcoholic solvents resulted in crystalline bimetallic oxide nanoparticles of various crystalline phases containing defects. In ethanol, bimodal crystalline Ni/Au BONs with median size of 15 nm were generated. In contrast, Ni/Au BONs with smaller median size and lower IQR were observed in isopropanol and butanol.

In butanol, high-resolution transmission electron microscopy revealed the encapsulation of Ni/Au BONs with a thin graphitic shell of a few atomic layers. Presumably, direct photolysis of butanol molecules by highly intense femtosecond laser pulses caused butanol disintegration to carbon species. Furthermore, laser-induced creation of supercritical temperature liquid due to the interaction of molten metallic layer of Ni/Au target with solvent may initiate butanol decomposition and generation of graphitic species.

The improved colloidal stability can be explained by two anticipated mechanisms. Firstly, the formation of graphite networks inside colloidal solution causes steric stabilization among nanoparticles. This can reduce particle diffusion, coagulation, Ostwald ripening processes, and agglomerations. Secondly, graphite deposition on laser-synthesized primary and secondary Ni/Au BONs may prevent particles from further diffusional growth.

High-intensity ultrashort laser pulses with moderate pulse repetition rates due to lower heat accumulation and

Table 7 The laser-synthesized Ni/Au BONs in butanol, selected area diffraction pattern results, corresponding crystallographic data and phase identifiers ($N = 1000$, $F = 1$ J cm^{-2})

Material	Crystal system	Lattice distance, nm	Miller indices	Pearson symbol	Space group	Space group number
Ni	Hexagonal	0.216	[002]	hP2	$P6_3/mmc$	194
Au	Cubic	0.203	[200]	cF4	Fm-3m	225
Ni	Hexagonal	0.203	[101]	hP2	$P6_3/mmc$	194
Au_2O_3	Orthorhombic	0.183	[022]	Fdd2	oF40	43
Au_2O_3	Orthorhombic	0.149	[551], [371]	Fdd2	oF40	43
NiO	Cubic	0.147	[220]	cF8	Fm-3m	225
NiO	Monoclinic	0.147	[111]	mS4	C2/m	12
NiO	Hexagonal	0.147	[110], [104]	hR6	R-3m	166
Ni	Cubic	0.124	[220]	cF4	Fm-3m	225
Ni	Hexagonal	0.115	[200]	hP2	$P6_3/mmc$	194
Ni	Cubic	0.106	[111]	cF4	Fm-3m	225

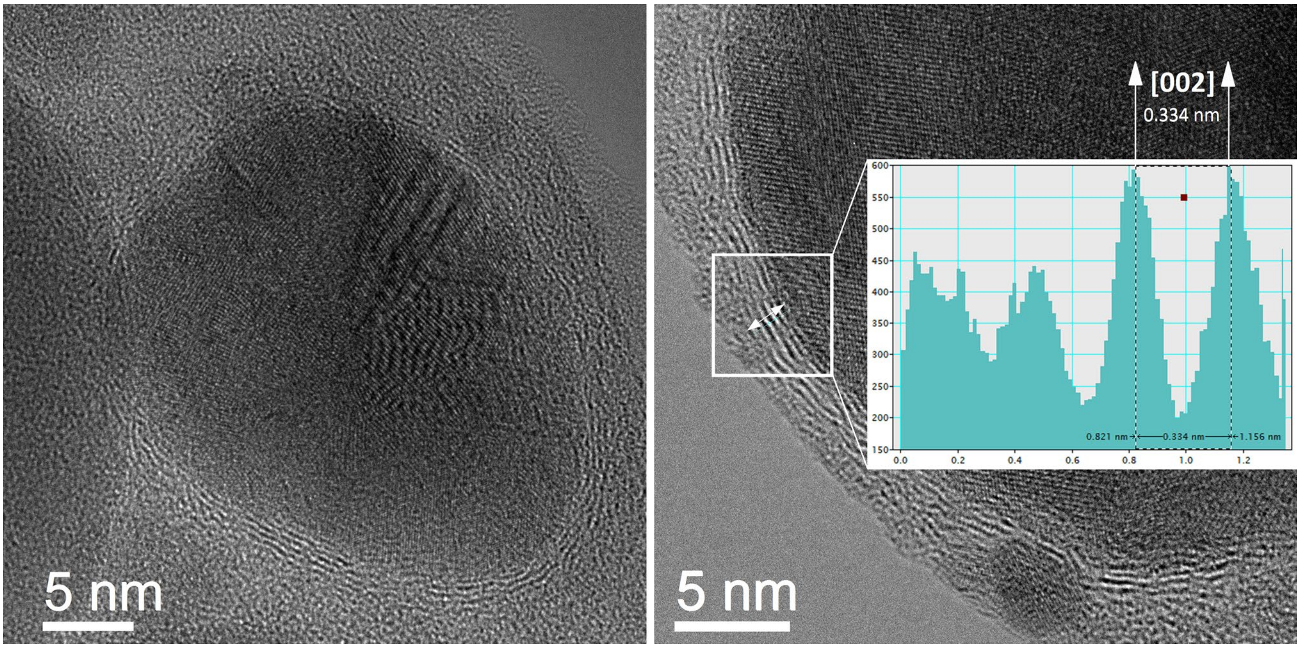

Fig. 11 The HRTEM of femtosecond laser-synthesized Ni/Au BONs in butanol and presented intensity profile along the arrow ($N = 1000$, $F = 1$ J cm^{-2})

subsequently less energy losses can generate localized material processing, better ablation efficiency, and productivity.

Acknowledgements Partial financial support for Ni/Au target preparation by physical chemistry department of Vienna University is gratefully acknowledged. The authors gratefully appreciate Prof. Dr. Herbert Hutter at surface analysis center for providing IONTOF system. The authors also acknowledge Dipl.-Ing. Fabian Bohrn for operating IONTOF and measuring gold thickness on nickel target.

References

1. D. Zhang, B. Gökce, S. Barcikowski, Laser synthesis and processing of colloids: fundamentals and applications. Chem. Rev. **117**, 3990–4103 (2017)
2. V.S.D. Oliveira, F.R. Henrique, I.L. Graff, W.H. Schreiner, J.A.G. Bezerra, Green synthesis of sub-10 nm gold nanoparticles by two-step laser irradiation. in *2012 Conference on Lasers and Electro-Optics (CLEO)*, San Jose, CA (2012), pp. 1–2
3. M.C. Sportelli, M. Izzi, A. Volpe, M. Clemente, R.A. Picca, A. Ancona, P.M. Lugarà, G. Palazzo, N. Cioffi, The pros and cons of the use of laser ablation synthesis for the production of silver nano-antimicrobials. Antibiotics (Basel, Switzerland) **7**, 67 (2018)

4. P.P. Patil, D.M. Phase, S.A. Kulkarni, S.V. Ghaisas, S.K. Kulkarni, S.M. Kanetkar, S.B. Ogale, V.G. Bhide, Pulsed-laser-induced reactive quenching at liquid–solid interface: aqueous oxidation of iron. Phys. Rev. Lett. **58**, 238–241 (1987)
5. F. Mafune, J.-Y. Kohno, Y. Takeda, T. Kondow, H. Sawabe, Formation and size control of silver nanoparticles by laser ablation in aqueous solution. J. Phys. Chem. B **104**, 9111–9117 (2000)
6. A.V. Kabashin, M. Meunier, Synthesis of colloidal nanoparticles during femtosecond laser ablation of gold in water. J. Appl. Phys. **94**, 7941–7943 (2003)
7. M. Brikas, S. Barcikowski, B. Chichkov, G. Račiukaitis, Production of nanoparticles with high repetition rate picosecond laser. J. Laser Micro Nanoeng. **2**, 230–233 (2007)
8. D. Bäuerle, *Laser processing and chemistry*, 4th edn. (Springer, Berlin, 2011)
9. S.C. Singh, H.B. Zeng, C. Guo, W. Cai, *Nanomaterials: Processing and Characterization with Lasers* (Wiley-VCH Verlag GmbH & Co. KGaA, Germany, 2012)
10. G. Yang, *Laser Ablation in Liquids, Principles and Applications in the Preparation of Nanomaterials* (Pan Stanford Publishing, Redwood, 2012)
11. S. Barcikowski, G. Compagnini, Advanced nanoparticle generation and excitation by lasers in liquids. Phys. Chem. Chem. Phys. **15**, 3022–3026 (2013)
12. N. Lasemi, U. Pacher, C. Rentenberger, O. Bomatí-Miguel, W. Kautek, Laser-assisted synthesis of colloidal Ni/NiO$_x$ core/shell nanoparticles in water and alcoholic solvents. ChemPhysChem **18**, 1118–1124 (2017)
13. N. Lasemi, O. Bomatí-Miguel, R. Lahoz, V.V. Lennikov, U. Pacher, C. Rentenberger, W. Kautek, Laser-assisted synthesis of colloidal FeW$_x$O$_y$ and Fe/Fe$_x$O$_y$ nanoparticles in water and ethanol. ChemPhysChem **19**, 1414–1419 (2018)
14. N. Najafianpour, D. Dorranian, Properties of graphene/Au nanocomposite prepared by laser irradiation of the mixture of individual colloids. Appl. Phys. A **124**, 805 (2018)
15. K.C. Phillips, H.H. Gandhi, E. Mazur, S.K. Sundaram, Ultrafast laser processing of materials: a review. Adv. Opt. Photonics **7**, 684–712 (2015)
16. S.K. Sundaram, E. Mazur, Inducing and probing non-thermal transitions in semiconductors using femtosecond laser pulses. Nat. Mater. **1**, 217 (2002)
17. G. Merga, L.C. Cass, D.M. Chipman, D. Meisel, Probing silver nanoparticles during catalytic H_2 evolution. J. Am. Chem. Soc. **130**, 7067–7076 (2008)
18. A. Corma, H. Garcia, Supported gold nanoparticles as catalysts for organic reactions. Chem. Soc. Rev. **37**, 2096–2126 (2008)
19. S.P. Murzin, G. Liedl, R. Pospichal, A.A. Melnikov, Study of the action of a femtosecond laser beam on samples of a Cu–Zn alloy. J. Phys. Conf. Ser. **1096**, 012138 (2018)
20. S.I. Anisimov, B.L. Kapeliovich, T.L. Perelman, Electron emission from metal surfaces exposed to ultrashort laser pulses. Sov. Phys. JETP **39**, 375 (1974)
21. Y.V. Afanasiev, B.N. Chichkov, N.N. Demchenko, V.A. Isakov, I.N. Zavestovskaia, Extended two-temperature model of laser ablation of metals. Proc. SPIE **4065**, 349–354 (2000)
22. K.-H. Leitz, B. Redlingshöfer, Y. Reg, A. Otto, M. Schmidt, Metal ablation with short and ultrashort laser pulses. Phys. Procedia **12**, 230–238 (2011)
23. L. Jiang, A.-D. Wang, B. Li, T.-H. Cui, Y.-F. Lu, Electrons dynamics control by shaping femtosecond laser pulses in micro/nanofabrication: modeling, method, measurement and application. Light Sci. Appl. **7**, 17134 (2018)
24. R.R. Letfullin, T.F. George, G.C. Duree, B.M. Bollinger, Ultrashort laser pulse heating of nanoparticles: comparison of theoretical approaches. Adv. Opt. Technol. **2008**, 8 (2008)
25. B.N. Chichkov, C. Momma, S. Nolte, F. von Alvensleben, A. Tünnermann, Femtosecond, picosecond and nanosecond laser ablation of solids. Appl. Phys. A **63**, 109–115 (1996)
26. S.M. Eaton, H. Zhang, P.R. Herman, F. Yoshino, L. Shah, J. Bovatsek, A.Y. Arai, Heat accumulation effects in femtosecond laser-written waveguides with variable repetition rate. Opt. Express **13**, 4708–4716 (2005)
27. P. Wagener, J. Jakobi, C. Rehbock, V.S.K. Chakravadhanula, C. Thede, U. Wiedwald, M. Bartsch, L. Kienle, S. Barcikowski, Solvent-surface interactions control the phase structure in laser-generated iron-gold core-shell nanoparticles. Sci. Rep. **6**, 23352 (2016)
28. G. Olivié, D. Giguère, F. Vidal, T. Ozaki, J.C. Kieffer, O. Nada, I. Brunette, Wavelength dependence of femtosecond laser ablation threshold of corneal stroma. Opt. Express **16**, 4121–4129 (2008)
29. D. Riabinina, M. Chaker, J. Margot, Dependence of gold nanoparticle production on pulse duration by laser ablation in liquid media. Nanotechnology **23**, 135603 (2012)
30. A. Vogel, J. Noack, G. Hüttman, G.J.A.P.B. Paltauf, Mechanisms of femtosecond laser nanosurgery of cells and tissues. Appl. Phys. B **81**, 1015–1047 (2005)
31. J. Noack, A. Vogel, Laser-induced plasma formation in water at nanosecond to femtosecond time scales: calculation of thresholds, absorption coefficients, and energy density. IEEE J. Quantum Electron. **35**, 1156–1167 (1999)
32. A. Hu, J. Sanderson, A.A. Zaidi, C. Wang, T. Zhang, Y. Zhou, W.W. Duley, Direct synthesis of polyyne molecules in acetone by dissociation using femtosecond laser irradiation. Carbon **46**, 1823–1825 (2008)
33. G. Bajaj, R.K. Soni, Effect of liquid medium on size and shape of nanoparticles prepared by pulsed laser ablation of tin. Appl. Phys. A **97**, 481–487 (2009)
34. P. Srinoi, Y.-T. Chen, V. Vittur, M.D. Marquez, T.R. Lee, Bimetallic nanoparticles: enhanced magnetic and optical properties for emerging biological applications. Appl. Sci. **8**(7), 1106 (2018). https://doi.org/10.3390/app8071106
35. L. Rout, A. Kumar, R.S. Dhaka, P. Dash, Bimetallic Ag–Cu alloy nanoparticles as a highly active catalyst for the enamination of 1,3-dicarbonyl compounds. RSC Adv. **6**, 49923–49940 (2016)
36. A. Neumeister, J. Jakobi, C. Rehbock, J. Moysig, S. Barcikowski, Monophasic ligand-free alloy nanoparticle synthesis determinants during pulsed laser ablation of bulk alloy and consolidated microparticles in water. Phys. Chem. Chem. Phys. **16**, 23671–23678 (2014)
37. J. Zhang, D.N. Oko, S. Garbarino, R. Imbeault, M. Chaker, A.C. Tavares, D. Guay, D. Ma, Preparation of PtAu alloy colloids by laser ablation in solution and their characterization. J. Phys. Chem. C **116**, 13413–13420 (2012)
38. D.D. Radev, Nickel-containing alloys for medical application obtained by methods of mechanochemistry and powder metallurgy. ISRN Metall **2012**, 6 (2012)
39. B.D. Chandler, C.G. Long, J.D. Gilbertson, C.J. Pursell, G. Vijayaraghavan, K.J. Stevenson, Enhanced oxygen activation over supported bimetallic Au–Ni catalysts. J. Phys. Chem. C **114**, 11498–11508 (2010)
40. L. Lang, Z. Pan, J. Yan, Ni–Au alloy nanoparticles as a high performance heterogeneous catalyst for hydrogenation of aromatic nitro compounds. J. Alloys Compd. **792**, 286–290 (2019)
41. S. Moradi, P.A. Azar, N. Lasemi, Preparation of nickel nanoparticles under ultrasonic irradiation. J. Appl. Chem. Res. **2**, 43–51 (2008)
42. C.-Y. Shih, C. Wu, M.V. Shugaev, L.V. Zhigilei, Atomistic modeling of nanoparticle generation in short pulse laser ablation of thin metal films in water. J. Colloid Interface Sci. **489**, 3–17 (2017)

43. D.M. Mattox, Physical vapor deposition (PVD) processes. Met. Finish. **98**, 410–423 (2000)
44. A. Fernandez, T. Fuji, A. Poppe, A. Fürbach, F. Krausz, A. Apolonski, Chirped-pulse oscillators: a route to high-power femtosecond pulses without external amplification. Opt. Lett. **29**, 1366–1368 (2004)
45. D. Strickland, G. Mourou, Compression of amplified chirped optical pulses. Opt. Commun. **56**, 219–221 (1985)
46. J.-C.M. Diels, J.J. Fontaine, I.C. McMichael, F. Simoni, Control and measurement of ultrashort pulse shapes (in amplitude and phase) with femtosecond accuracy. Appl. Opt. **24**, 1270–1282 (1985)
47. Y. Jee, M.F. Becker, R.M. Walser, Laser-induced damage on single-crystal metal surfaces. J. Opt. Soc. Am. B **5**, 648–659 (1988)
48. M. Wollenhaupt, A. Assion, T. Baumert, Short and ultrashort laser pulses, in *Springer Handbook of Lasers and Optics*, ed. by F. Träger (Springer, Berlin, 2012), pp. 1047–1094
49. X. Yibin, Y. Masayoshi, V. Pierre, Inorganic materials database for exploring the nature of material. Jpn. J. Appl. Phys. **50**, 11RH02 (2011)
50. A. De Giacomo, M. Dell'Aglio, A. Santagata, R. Gaudiuso, O. De Pascale, P. Wagener, G.C. Messina, G. Compagnini, S. Barcikowski, Cavitation dynamics of laser ablation of bulk and wire-shaped metals in water during nanoparticles production. Phys. Chem. Chem. Phys. **15**, 3083–3092 (2013)
51. M.-R. Kalus, N. Barsch, R. Streubel, E. Gokce, S. Barcikowski, B. Gokce, How persistent microbubbles shield nanoparticle productivity in laser synthesis of colloids—quantification of their volume, dwell dynamics, and gas composition. Phys. Chem. Chem. Phys. **19**, 7112–7123 (2017)
52. A. Hahn, S. Barcikowski, B.N. Chichkov, Influences on nanoparticle production during pulsed laser ablation. J. Laser Micro Nanoeng. **3**, 73–77 (2008)
53. E. Whitley, J. Ball, Statistics review 1: presenting and summarising data. Crit. Care **6**, 66–71 (2002)
54. P. Wagener, S. Ibrahimkutty, A. Menzel, A. Plech, S. Barcikowski, Dynamics of silver nanoparticle formation and agglomeration inside the cavitation bubble after pulsed laser ablation in liquid. Phys. Chem. Chem. Phys. **15**, 3068–3074 (2013)
55. S. Ibrahimkutty, P. Wagener, A. Menzel, A. Plech, S. Barcikowski, Nanoparticle formation in a cavitation bubble after pulsed laser ablation in liquid studied with high time resolution small angle X-ray scattering. Appl. Phys. Lett. **101**, 103104 (2012)
56. S. Ibrahimkutty, P. Wagener, T.D.S. Rolo, D. Karpov, A. Menzel, T. Baumbach, S. Barcikowski, A. Plech, A hierarchical view on material formation during pulsed-laser synthesis of nanoparticles in liquid. Sci. Rep. **5**, 16313 (2015)
57. C. Gammer, C. Mangler, C. Rentenberger, H.P. Karnthaler, Quantitative local profile analysis of nanomaterials by electron diffraction. Scripta Mater. **63**, 312–315 (2010)
58. J.A. Kittl, P.G. Sanders, M.J. Aziz, D.P. Brunco, M.O. Thompson, Complete experimental test for kinetic models of rapid alloy solidification. Acta Mater. **48**, 4797–4811 (2000)
59. M. Bienzle, T. Oishi, F. Sommer, Thermodynamics and local atomic arrangements of gold-nickel alloys. J. Alloys Compd. **220**, 182–188 (1995)
60. A.A. Ilyin, S.S. Golik, Femtosecond laser-induced breakdown spectroscopy of sea water. Spectrochim. Acta Part B **87**, 192–197 (2013)
61. V. Amendola, G.A. Rizzi, S. Polizzi, M. Meneghetti, Synthesis of gold nanoparticles by laser ablation in toluene: quenching and recovery of the surface plasmon absorption. J. Phys. Chem. B **109**, 23125–23128 (2005)
62. M.G. John, K.M. Tibbetts, One-step femtosecond laser ablation synthesis of sub-3 nm gold nanoparticles stabilized by silica. Appl. Surf. Sci. **475**, 1048–1057 (2019)
63. O. Baranov, S. Xu, K. Ostrikov, B.B. Wang, U. Cvelbar, K. Bazaka, I. Levchenko, Towards universal plasma-enabled platform for the advanced nanofabrication: plasma physics level approach. J. Rev. Mod. Plasma Phys. **2**, 4 (2018)
64. I. Levchenko, K. Bazaka, M. Keidar, S. Xu, J. Fang, Hierarchical multicomponent inorganic metamaterials: intrinsically driven self-assembly at the nanoscale. Adv. Mater. **30**, 1702226 (2018)
65. V. Amendola, M. Meneghetti, Laser ablation synthesis in solution and size manipulation of noble metal nanoparticles. Phys. Chem. Chem. Phys. **11**, 3805–3821 (2009)
66. V. Amendola, P. Riello, M. Meneghetti, Magnetic nanoparticles of iron carbide, iron oxide, iron@iron oxide, and metal iron synthesized by laser ablation in organic solvents. J. Phys. Chem. C **115**, 5140–5146 (2011)
67. H.Y. Kwong, M.H. Wong, C.W. Leung, Y.W. Wong, K.H. Wong, Formation of core/shell structured cobalt/carbon nanoparticles by pulsed laser ablation in toluene. J. Appl. Phys. **108**, 034304 (2010)
68. G. Cristoforetti, E. Pitzalis, R. Spiniello, R. Ishak, F. Giammanco, M. Muniz-Miranda, S. Caporali, Physico-chemical properties of Pd nanoparticles produced by pulsed laser ablation in different organic solvents. Appl. Surf. Sci. **258**, 3289–3297 (2012)
69. V.Y. Bychkov, Y.P. Tyulenin, A.A. Firsova, E.A. Shafranovsky, A.Y. Gorenberg, V.N. Korchak, Carbonization of nickel catalysts and its effect on methane dry reforming. Appl. Catal. A **453**, 71–79 (2013)
70. N. Lasemi, U. Pacher, L.V. Zhigilei, O. Bomatí-Miguel, R. Lahoz, W. Kautek, Pulsed laser ablation and incubation of nickel, iron and tungsten in liquids and air. Appl. Surf. Sci. **433**, 772–779 (2018)
71. A. Lima da Silva, I.L. Müller, Hydrogen production by sorption enhanced steam reforming of oxygenated hydrocarbons (ethanol, glycerol, *n*-butanol and methanol): thermodynamic modelling. Int. J. Hydrog. Energy **36**, 2057–2075 (2011)
72. D. Werner, S. Hashimoto, T. Tomita, S. Matsuo, Y. Makita, Examination of silver nanoparticle fabrication by pulsed-laser ablation of flakes in primary alcohols. J. Phys. Chem. C **112**, 1321–1329 (2008)